

# Impact of non-ideal behavior on ignition delay and chemical kinetics in high-pressure shock tube reactors

Gandhali Kogekar<sup>a</sup>, Canan Karakaya<sup>a</sup>, Gary J. Liskovich<sup>b</sup>, Matthew A. Oehlschlaeger<sup>b</sup>, Steven C. DeCaluwe<sup>a,\*</sup>, Robert J. Kee<sup>a</sup>

<sup>a</sup>Department of Mechanical Engineering, Colorado School of Mines, Golden, CO 80401, USA

<sup>b</sup>Department of Mechanical, Aerospace, and Nuclear Engineering, Rensselaer Polytechnic Institute, Troy, NY 12180, USA

---

## Abstract

Here, we study real gas effects on high-pressure combustion by comparing simulated and experimentally-measured shock tube ignition delay measurements for n-dodecane/O<sub>2</sub>/N<sub>2</sub> mixtures. Experiments and simulations occur at conditions relevant to diesel engines: 40–80 atm, 774–1163 K, equivalence ratios of 1.0 and 2.0, and O<sub>2</sub> concentrations of 13–21%. At these conditions the fuel, oxidizer and intermediate species may exist in a supercritical state during combustion, requiring a real gas equation of state to incorporate non-ideal effects on thermodynamics, chemical kinetics, and the resulting ignition characteristics. A constant-volume, adiabatic reactor model is developed to simulate the reflected shock tube experiments, and simulations compare results for real and ideal gas equations of state, with different expressions for reacting species' activity concentrations. This paper focuses particularly on the cubic Redlich–Kwong equation of state and thermodynamically consistent chemical kinetic rate calculations based on it. Results demonstrate that the equation of state can have considerable influence on ignition delay times with increasing pressure, particularly in the negative temperature coefficient region. Additionally, the results establish important practices for incorporating real gas effects, namely that (i) the compressibilities of key species (i.e. those participating in rate-limiting reactions) are the appropriate way to screen for real gas effects, rather than the average mixture compressibility; and (ii) incorporating a real gas equation of state without also incorporating thermodynamically consistent chemical kinetics significantly under-predicts the magnitude of real gas effects.

**Keywords:** Shock tube reactor, High-pressure combustion, Redlich–Kwong equation of state, Real gas effects, CANTERA, Negative temperature coefficient

---

## 1. Introduction

With the increasing relevance of high operating pressures for numerous combustion technologies, including diesel engines, jet propulsion, gas turbines and fuel injectors, understanding real gas effects on combustion performance becomes increasingly important. Simulation and analysis of high-pressure combustion (usually, more than 10 atm)—where major species experience trans-critical and supercritical states—must incorporate non-idealities in thermodynamic and chemical kinetic properties, which are highly susceptible to even small fluctuations in pressure and temperature near the critical point. While real gas models have been common

in the literature for many decades [1–3], their application to complex combustion simulations remains limited. As such, conventions for their adoption and use in the combustion field are not well defined, which can be the source of confusion, error, and inconsistency in their application.

The present paper focuses on real gas effects in reflected shock tube experiments at supercritical pressures. Achieving conditions found in internal combustion and gas turbine engines in controlled experimental reactors or flames is not trivial, and often kinetic models are not tested against target data at the conditions for which the models are eventually employed. Recent collaborative efforts within the Engine Combustion Network (ECN) [4] seek to exhaustively characterize canonical spray ignition and combustion experiments at realistic compression-ignition engine conditions and model those experiments using computational fluid dy-

---

\*Corresponding author. Tel: +1-303-273-3666.

Email address: decaluwe@mines.edu (Steven C. DeCaluwe)

namics. One such canonical experiment is the Sandia Spray A [4], where the baseline condition is n-dodecane injection into an ambient gas at temperature of 900 K, density of  $22.8 \text{ kg m}^{-3}$  (ca. 60 atm), and containing 15%  $\text{O}_2$ . Perturbations in temperature, density/pressure,  $\text{O}_2$  concentration, injection parameters, and fuel have been widely studied experimentally within the ECN in both the Spray A and other configurations [5–7]. Additionally, ignition delay studies for n-dodecane [8–11] have been carried out in shock tubes, but few studies approach the conditions found in the n-dodecane Spray A experiment. Lastly, autoignition experiments have been reported for n-decane in both shock tubes [10, 12, 13] and rapid compression machines [14], with two notable shock tube studies reporting ignition delay at high-pressure engine conditions. Pfahl et al. [12] measured ignition delay times (IDTs) for  $\phi=0.5\text{--}2$  n-decane/air mixtures at 13–50 atm and 700–1300 K, and Zhukov et al. [13] reported ignition delay for  $\phi=0.5\text{--}1$  n-decane/air mixtures at 10–80 atm and 800–1300 K.

Real gas effects in high-pressure combustion have been studied in individual efforts over the past several decades [15, 16]. Li et al. [17] developed CHEMShock, a shock tube modeling tool that includes facility dependent non-idealities such as incident-shock attenuation and boundary layer growth [15]. Sivaramakrishnan et al. [18], used non-Arrhenius rate parameters to incorporate real gas effects. Davidson and Hanson [19] modeled real gas shock wave equations using the Peng–Robinson [3] equation of state (EoS), and analyzed real gas effects in kinetics and reaction pathways. Schmitt, et al.’s CHEMKin REAL GAS package [20] extends CHEMKin-II [21] with custom code to incorporate several cubic real gas EoS types, and has been used in subsequent studies to understand real gas effects on detonation properties of gases at high pressures [22]. Tang and Brezinsky [23] used CHEMKin REAL GAS’s Peng–Robinson [3] EoS to demonstrate the impacts of pressure and temperature variations, common assumptions about the quenching process, and non-ideality on the reaction conditions behind high pressure reflected shock waves. They present a set of equations to describe the impact of non-ideality on  $p - v - T$  relationships, thermodynamic properties, and chemical kinetics, and consider the impact of non-ideality on the chemical rate coefficients themselves. Hanson and Petersen [24] use the Peng–Robinson EoS to extend the GRI-Mech 1.2 thermokinetic mechanism for high-pressure combustion of low-dilution methane-oxygen mixtures, validated against experimental IDT data. Despite the value of these studies, adoption of their insights and further study of real gas effects in high-pressure combustion has

been limited. Experimental ignition delay studies to validate the kinetic models used in high-pressure combustion simulations are currently lacking, and in most cases the kinetic treatments of high-pressure reacting mixtures assume ideal gas behavior. Many models utilize commercial ANSYS CHEMKin-PRO [25] software, which implements an ideal gas EoS [26, 18, 27].

In this paper, simulated high-pressure shock tube results are compared to experimental data to (i) estimate the magnitude of non-ideal effects and (ii) establish conventions for incorporating real gas effects in future studies. New shock tube ignition delay measurements are reported for n-dodecane at the conditions encompassing the very high pressures found in the Sandia Spray A experiment. The present condition space has been chosen to cover a parametric variation of pressure, temperature, and oxygen concentration considered within the spray experiments and provides data at fuel-rich conditions where local ignition within typical spray environments occurs. Of particular interest in this paper is Negative Temperature Coefficient (NTC) behavior at intermediate temperatures, where observed IDTs increase with increasing temperature. IDT and NTC phenomena have been explored in low-pressure studies for applications such as diesel sprays [28] and oxy-methane combustion [29, 30], but the effects of non-ideal behavior at high pressures have not been studied in detail.

Numerical simulations in this work follow an approach similar to Schmitt, et al. [20], Tang and Brezinsky [23], and Hanson and Petersen [24], but employ the Redlich-Kwong (R-K) [1] EoS available in CANTERA [31], rather than the Peng–Robinson equation, to model real gas effects on shock tube ignition. The work by Tang and Brezinsky discusses, in considerable detail, real gas effects in the high pressure shock tube combustion of stoichiometric ethane/air, including endwall temperature measurement, species mole fraction profiles, and reaction pathway sensitivity. We extend this previous work to consider the real gas effects on IDTs for n-dodecane/air in the NTC region, and demonstrate the magnitude of common errors, such as neglecting the impact of real gas effects on  $p - v - T$  behavior and chemical kinetics, on predicted IDT values. Another goal of the current study is to encourage greater adoption of non-ideal EoS by modelers and experimentalists alike. As such, we lay out a clear and unambiguous description of the relevant equations, which can readily be extended to other EoS, and concurrently make available a free, open-source version of the simulation tool used herein.

Simulated IDTs are compared to the experimental data and demonstrate the impact of a real gas EoS

(i.e., ideal gas law versus a multi-component R–K formulation) and mass activity formulations (i.e., activity concentrations expressed as molar concentrations versus calculated via species activities). Results demonstrate that non-ideal behavior can affect predicted IDTs by as much as 50–100  $\mu\text{s}$  in the NTC region, and that implementing a real gas thermodynamic model without also incorporating real gas chemical kinetic effects significantly under-predicts real gas effects. Results also demonstrate that the average compressibility of a mixture is an insufficient metric for determining real gas effects, which can be important even in cases where the average mixture behaves as an ideal gas (i.e. when the compressibility is very close to one). Rather than the mixture compressibility, the compressibility of key species—those participating in rate-limiting reaction steps—must be evaluated in order to predict the importance of real gas effects.

## 2. Methods

### 2.1. Shock tube reactor model

Following the example of Schmitt et al.[20], reflected shock tube experiments are modeled as a zero-dimensional, constant-volume, adiabatic reactor. The computational model is implemented in MATLAB<sup>1</sup>, and uses CANTERA—an open-source software tool for chemical kinetics, species transport, and thermodynamics calculations—to manage thermo-kinetic calculations [31]. CANTERA’s object-oriented nature, and the associated class inheritance characteristics, make it easily extensible, such that real gas models can be incorporated efficiently while also preserving higher-level functionality common to multiple EoS formulations.

The applicable governing equations for energy and species conservation for a constant volume, adiabatic reactor, can be expressed as:

$$\frac{du}{dt} = 0 \quad (1)$$

and

$$\frac{d}{dt}[X_k] = \dot{\omega}_k. \quad (2)$$

In the above equations,  $[X_k]$  is the molar concentration ( $\text{mol}_k \text{ m}^{-3}$ ),  $t$  is time,  $\dot{\omega}_k$  is the net production rate of  $k^{\text{th}}$  species due to chemical reactions ( $\text{mol}_k \text{ m}^{-3} \text{ s}^{-1}$ ), and  $u$  is the specific internal energy of the mixture, per unit mass ( $\text{J kg}^{-1}$ ), calculated as:

$$u = \sum_k Y_k u_k, \quad (3)$$

where  $Y_k$  and  $u_k$  represent the mass fraction and specific internal energy ( $\text{J kg}_k^{-1}$ ), respectively, of species  $k$ . These governing equations form a transient system of ordinary differential-algebraic equations, which are solved using the function `ode15s` in the MATLAB ODE suite [32]. To solve Eq. 2, CANTERA functions are called at every timestep to update species chemical production rates ( $\dot{\omega}_k$ ) and other thermodynamic properties. Eqs. 1 and 3 are solved algebraically for a given chemical composition, to identify the temperature  $T$  such that specific internal energy  $u$  remains constant at every time step.

The species chemical production rates ( $\dot{\omega}_k$ ) are evaluated using a detailed reaction mechanism for n-dodecane oxidation developed by Wang et al. [33]. This reaction mechanism includes 432 reactions among 100 species, with an Arrhenius rate expression specified for each reaction. Pressure-dependent reactions are represented using the Chebyshev polynomial formulation. Each reaction is assumed to be microscopically reversible, with the reverse rate evaluated from the forward rate and the equilibrium constant. Species are named using the SMILES (Simplified molecular-input line-entry system) convention.

### 2.2. Reflected shock tube experiments

Ignition delay measurements were performed for n-dodecane/air in the Rensselaer heated high-pressure shock tube using the reflected shock technique; see Shen et al. [34] and Wang et al. [35] for details of the experimental setup and ignition delay measurement technique. In the present experiments, n-dodecane at 99+% purity (*Sigma Aldrich*) and  $\text{O}_2$  and  $\text{N}_2$  at 99.995% purity (*Noble Gas*) were used. The reactant mixtures studied are defined in Table 1 and include stoichiometric and rich ( $\phi=2$ ) conditions, fuel-air mixtures (21%  $\text{O}_2$ ) and dilute mixtures emulative of in-cylinder mixtures containing exhaust gas recirculation, pressures from 40 to 80 atm, and temperatures that span the low- to high-temperature ignition regimes. The shock tube, reactant mixing vessel, and gas transfer lines were uniformly heated to temperatures from 160 to 180 °C using an electric heating system to ensure sufficient partial pressure of n-dodecane at the range of variable initial conditions required to achieve the desired reflected shock conditions listed in Table 1.

Ignition delay times were determined behind reflected shock waves using a combination of pressure and  $\text{OH}^*$  chemiluminescence [34, 35]. An example ignition delay measurement is provided in Fig.1. For temperatures within the low-temperature and the lower temperature portion of the NTC regime, two-stage ignition was observed (cf. Fig. 1) where the pressure clearly shows

<sup>1</sup>The MathWorks, Inc; Natick, MA,USA; [www.mathworks.com](http://www.mathworks.com)

Table 1: Experimental conditions for n-dodecane/O<sub>2</sub>/N<sub>2</sub> ignition delay measurements.

n-dodecane [mol-%]	O <sub>2</sub> [mol-%]	N <sub>2</sub> [mol-%]	$\phi$	$p$ [atm]	$T$ [K]
1.12	20.77	78.10	1.0	40, 60, 80	775–1160
2.22	20.54	77.24	2.0	40, 60	800–1120
0.811	15.00	84.19	1.0	60	840–1110
0.703	13.00	86.30	1.0	60	840–1140

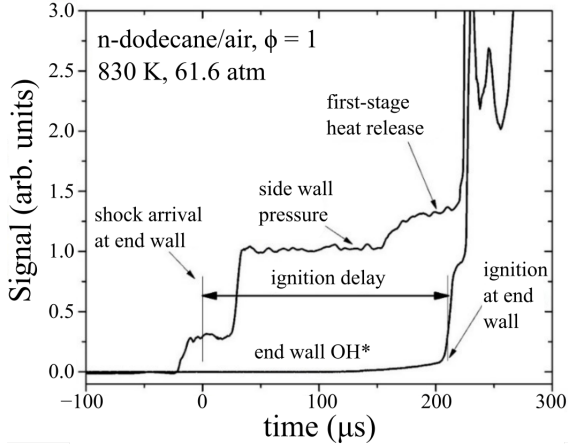


Figure 1: Example pressure and OH\* chemiluminescence signals for a stoichiometric n-dodecane/air ignition delay measurement.

first-stage ignition followed by an induction period to a very strong second-stage hot ignition.

In the present work, the normalized pressure rise following the reflected shock heating, due to viscous gas dynamics, was in the range of  $dp/dt = 2\text{--}5\%$   $\text{ms}^{-1}$ . However, the calculated IDTs are negligibly influenced by this pressure rise because ignition delay times are relatively short ( $< 1$  ms) at the high-pressure conditions considered. Hence, this pressure gradient was not considered in the kinetic modeling comparisons presented in the following sections. The temperature and pressure behind the reflected shock wave were determined using the normal shock equations (conservation of mass, momentum, and energy), solved in combination with the both a Redlich–Kwong [1] and Peng–Robinson [3] EoS, in the manner described by Davidson and Hanson [19]. At the highest pressure considered (80 atm), a non-ideal EoS results in a 4 K difference in calculated reflected shock temperature, relative to an ideal gas assumption. As demonstrated below, this does not imply that non-ideal effects on the combustion dynamics are negligible, only that the average thermodynamic properties of the mixture (including the N<sub>2</sub> bath gas) do not deviate significantly from the ideal gas approximation.

The uncertainties in reflected shock temperature and

pressure are estimated at  $\pm 1.0\text{--}1.5\%$  and  $\pm 1.5\text{--}2.0\%$ , respectively. Uncertainties in conditions, fuel/oxidizer mixture fractions, and determinations of ignition delay from the measured signals lead to an estimated uncertainty of  $\pm 20\%$  in the reported ignition delays. All ignition delay measurements are tabulated in the Appendix.

### 3. Ideal and real gas equations of state

The present study focuses on the effects of different EoS formulations on the ignition characteristics. In this paper, we have considered two EoS, viz. ideal gas and Redlich–Kwong (R–K). The behavior of gases is commonly expressed using the ideal gas law, which supposes equal molar volume for all species and no interaction potential between molecules:

$$p = \frac{RT}{v}, \quad (4)$$

where  $p$  is the pressure (Pa),  $R$  is the universal gas constant ( $\text{J mol}^{-1} \text{K}^{-1}$ ),  $T$  the temperature (K), and  $v$  the molar volume ( $\text{m}^3 \text{mol}^{-1}$ ). Although the ideal gas EoS shows satisfactory behavior at high temperatures and low pressures, thermodynamic properties near the critical point depart significantly from ideal behavior, due to intermolecular forces and molecular volumes that vary from species to species. The deviation from ideal behavior is typically measured in terms of the compressibility factor  $Z$ , defined as:

$$Z = \frac{pv}{RT}. \quad (5)$$

For an ideal gas,  $Z = 1$ . But at low temperatures and high pressures,  $T_r < 2$  and  $p_r > 0.5$ , respectively, the compressibility factor departs from unity. A great many non-ideal EoS have been described in the literature [1–3, 36–38]. Commonly, cubic equations of state—which are relatively straightforward to use and employ only 2–3 parameters—are used to model real gas effects. This approach was first introduced by Van der Waals in 1873 [36], and extended by Redlich and Kwong in 1949 [1]. Although the R–K EoS gives qualitatively accurate results across a range of non-ideal states, its

accuracy suffers in the liquid-vapor equilibrium region. Subsequent efforts have addressed this by modifying the original R–K formulation. Modifications by Soave [2] and Peng and Robinson [3] improve the accuracy in the region of the liquid-vapor phase transition by incorporating an additional parameter based on the acentric factor  $\omega$ . Aungier [37] developed an EoS using  $\omega$  and critical compressibility  $Z_c$  as additional parameters.

Beyond the cubic EoS forms above, multi-parameter formulations show even greater accuracy. For example, the multi-parameter Helmholtz energy EoS [38] is generally considered the most accurate, particularly for trans-critical processes (those where conditions move between sub- and super-critical states). However, thermodynamic calculations in this EoS are computationally expensive, relying on roughly 60 parameters. Moreover, the required parameters are available only for certain stable species and not for short-lived, reactive intermediates and radicals, making the Helmholtz EoS challenging for detailed chemistry and large-scale computational fluid dynamics simulations.

### 3.1. Redlich–Kwong equation of state

The present study uses a multi-component, mixture-averaged form of the R–K EoS [1] to predict real gas behavior. For a pure species, the R–K EoS is:

$$p = \frac{RT}{v - b^*} - \frac{a^*}{v \sqrt{T}(v + b^*)}. \quad (6)$$

Here, the species-specific Van der Waals attraction parameter  $a^*$  and repulsive volume correction parameter  $b^*$  represent the influence of molecular interactions. By definition, the R–K EoS assumes a critical compressibility  $Z_c=1/3$ :

$$Z_c = \frac{p_c v_c}{RT_c} = \frac{1}{3}, \quad (7)$$

where  $T_c$ ,  $p_c$ , and  $v_c$  are the critical temperature, pressure and molar volume for the species of interest, respectively. This allows direct calculation of the parameters  $a^*$  and  $b^*$ , based on the critical properties  $T_c$  and  $p_c$  [39].

For mixtures, the mixture-averaged parameters  $a_{\text{mix}}^*$  and  $b_{\text{mix}}^*$  can be evaluated using mixing rules as [40]:

$$a_{\text{mix}}^* = \sum_i \sum_j X_i X_j a_{ij}^*, \quad (8)$$

and:

$$b_{\text{mix}}^* = \sum_i X_i b_i^*. \quad (9)$$

where  $X_k$  is the mole fraction of species  $k$ . In the absence of experimental data to guide parameter estimation, the interaction parameter  $a_{ij}^*$  is evaluated as the geometric average of the pure-species parameters and is given by [39]

$$a_{ij}^* = \sqrt{a_i^* a_j^*}. \quad (10)$$

In Eqs. 9 and 10,  $a_k^*$  and  $b_k^*$  are the pure-species parameters.

The goals of the present paper are to establish the magnitude of real gas effects on reflected shock tube IDTs at high pressure, and enable wider consideration of real gas effects in high-pressure combustion experiments and simulations. These goals are supported by the use of the multi-component Redlich–Kwong EoS in CANTERA. While alternate EoS such as Peng–Robinson provide greater accuracy in the liquid-vapor region, this implementation is not currently available in CANTERA. Moreover, the simulations herein probe conditions far from saturation, where the various EoS forms are expected to give roughly equivalent performance. This is demonstrated in Table 2, which lists the reduced properties and compressibility for the major species at the conditions closest to saturation (lowest  $T$ , highest  $p$ ). The major species are in general quite far from the critical point (from Eq. 7,  $Z_c = 1/3$  for the R–K EoS) and from the saturation region, namely because  $\text{H}_2\text{O}$  has a very high critical pressure, and n-dodecane has a relatively low critical pressure. The ability to readily modify the EoS implementation and to freely distribute the modeling tools used herein by using CANTERA therefore justify the minor loss of accuracy that accompanies the original R–K EoS.

#### 3.1.1. Critical property estimation: the Joback method

The  $a^*$  and  $b^*$  parameters in R–K EoS (Eq. 6) must be known or estimated for each species in the reaction mechanism. These parameters depend on a species's critical temperature and critical pressure, which are readily available for most stable species, but not for the many intermediate species and radicals included in most chemical mechanisms (including the present mechanism). In such cases, estimation methods such as those from Ambrose [41, 42], Joback [43, 44], and Fedors [45] are used. The present study uses the group contribution Joback method to estimate critical temperature ( $T_c$ ), critical pressure ( $p_c$ ), and boiling point ( $T_b$ ).

The Joback method uses a combination of basic structural properties for each chemical group within an individual species. The properties of a compound are functions of structurally dependent parameters, and are determined by summing the frequency of each group in the

Table 2: Critical and reduced temperatures and pressures and compressibilities for major species, at  $p = 80$  atm and  $T = 850$  K. Analysis justifies the use of the Redlich-Kwong EoS.

Species	$T_c$ [K]	$p_c$ [atm]	$T_r$ (at 850 K)	$p_r$ (at 80 atm)	$Z$ at 850 K, 80 atm
N <sub>2</sub>	126.2	33.5	6.7	2.4	1.02
CO <sub>2</sub>	304.2	72.9	2.8	1.1	1.00
H <sub>2</sub> O	647.1	217.7	1.3	0.4	0.94
O <sub>2</sub>	154.6	49.7	5.5	1.6	1.02
C <sub>12</sub> H <sub>26</sub> (fuel)	659.5	18.1	1.3	4.4	0.72

molecule multiplied by its contribution. The method assumes that interactions between groups are negligible, and is valid for polar and non-polar species. Owczarek and Blazej tabulated critical temperatures for a range of gases using multiple approaches [46, 47], and found that the Joback method limited errors to less than 1.5% for a range of branched and unbranched hydrocarbons.

The boiling-point temperature may be evaluated using the Joback method as:

$$T_{b,k}(\text{K}) = 198 + \sum_i N_i C_{T_{b,i}} \quad (11)$$

Subsequently, the ratio between the critical and boiling point temperatures  $T_{c,k}$  and  $T_{b,k}$  is estimated as:

$$\frac{T_{b,k}(\text{K})}{T_{c,k}(\text{K})} = 0.584 + 0.965 \left[ \sum_i N_i C_{T_{c,i}} \right] - \left[ \sum_i N_i C_{T_{c,i}} \right]^2, \quad (12)$$

while the critical pressure is calculated as:

$$p_{c,k}(\text{bar}) = \left[ 0.113 + 0.0032 N_{\text{atoms}} - \sum_i N_i C_{p_{c,i}} \right]^{-2}. \quad (13)$$

In these expressions, the index  $i$  indicates the group type, and  $N_i$  indicates the total number of  $i$  groups in the compound. Each group type  $i$  has a contribution to the critical temperature ( $C_{T_{c,i}}$ ), the boiling-point temperature ( $C_{T_{b,i}}$ ) and the critical pressure ( $C_{p_{c,i}}$ ). In Eq. 13,  $N_{\text{atoms}}$  indicates the total number of atoms in the compound. In the present study, all group contributions ( $C_{T_{c,i}}$ ,  $C_{T_{b,i}}$ ,  $C_{p_{c,i}}$ ) are taken from Reid et al. [39]

Group contribution parameters for short-lived species and radicals are generally not available. However, they may be estimated as equal to those of analogous stable species. For example, properties for the ethyl radical (C<sub>2</sub>H<sub>5</sub>) may be approximated using those of ethane (C<sub>2</sub>H<sub>6</sub>). Although the procedure has been applied successfully for high-pressure combustion studies, the accuracy for supercritical fluids with significant departures from ideal behavior is less clear.

### 3.1.2. Thermodynamic properties

One advantage of the R–K EoS (and other cubic EoS) is that thermodynamically consistent expressions can be derived for accurate properties across a wide range of states and phases, with low computational cost and only a few input parameters. The first step is to evaluate the molar Helmholtz free energy  $a$ , using its definition and integrating the equation of state. The molar Helmholtz free energy for given phase is defined via:

$$p \equiv - \left( \frac{\partial a}{\partial v} \right)_{n_k, T}, \quad (14)$$

where  $n_k$  is the number of moles of each species  $k$  (mol <sub>$k$</sub> ) and  $a$  is the molar Helmholtz energy (J mol<sup>-1</sup>) of the mixture. Thermodynamic properties are typically calculated relative to those for some well-known reference state, which here is chosen to be an ideal gas at the given temperature and chemical composition, but at a reference pressure  $p^\circ$  in the ideal gas regime. Integrating from this reference state to some general state yields the Helmholtz departure function:

$$a - a^\circ = \int_{a^\circ}^a da = - \int_{v^\circ}^v p dv = - \int_{\infty}^v p dv - \int_{v^\circ}^{\infty} p dv., \quad (15)$$

where the  $\infty$  represents compression from an infinite molar volume. The R–K EoS is used to substitute for the pressure in the first integral. The second integral resides entirely in the ideal gas regime, and hence the ideal gas EoS is substituted in for the pressure in this term:

$$(a - a^\circ) = - \int_{\infty}^v \frac{RT}{v - b_{\text{mix}}^*} dv + \int_{\infty}^v \frac{a_{\text{mix}}^*}{v \sqrt{T}(v + b_{\text{mix}}^*)} dv - \int_{v^\circ}^{\infty} \frac{RT}{v} dv. \quad (16)$$

After evaluating the integrals, utilizing the fact that  $\ln(1) = 0$ , and collecting terms, we arrive at:

$$(a - a^\circ) = -RT \ln \left( \frac{v - b_{\text{mix}}^*}{v^\circ} \right) - \frac{a_{\text{mix}}^*}{b_{\text{mix}}^* \sqrt{T}} \ln \left( \frac{v + b_{\text{mix}}^*}{v} \right) \quad (17)$$

where  $v^\circ$  is the reference state volume approximation, calculated according to the ideal gas assumption at the adopted reference pressure  $p^\circ$ .

$$(a - a^\circ) = -RT \ln \left( \frac{p^\circ (v - b_{\text{mix}}^*)}{RT} \right) - \frac{a_{\text{mix}}^*}{b_{\text{mix}}^* \sqrt{T}} \ln \left( \frac{v + b_{\text{mix}}^*}{v} \right) \quad (18)$$

This expression is equivalent to that outlined by Prausnitz et al. [48], excepting the  $p^\circ$  in the first logarithmic term, which is required to ensure that the term is dimensionless.

The reference state Helmholtz energy  $a_i^\circ(T)$  in Eq. 18 is defined as  $(u_k^\circ - T s_k^\circ)$ , with the species-specific reference state internal energy  $u_k^\circ$  and entropy  $s_k^\circ$  evaluated at the adopted reference state (an ideal gas at  $p^\circ$ ,  $T$ , and chemical composition  $X_k$ ). In the present study, these reference properties are calculated using standard-state, temperature-dependent properties  $u_k^\ddagger$  and  $s_k^\ddagger$ , which in turn are evaluated via NASA polynomials [49, 21] (i.e.  $u_k^\circ(T, X_k) = u_k^\ddagger(T)$ , and  $s_k^\circ(T, X_k) = s_k^\ddagger(T) - R \ln(X_k)$ ). Once the Helmholtz energy is available via Eq. 18, other thermodynamic properties such as specific entropy ( $s$ ), specific internal energy ( $u$ ), specific enthalpy ( $h$ ) and specific Gibb's free energy ( $g$ ) can be calculated easily using their relationship to the Helmholtz energy.

### 3.2. Chemical kinetics of real gases

#### 3.2.1. Real gas effects on mass action kinetics

As high-pressure (and hence non-ideal) experiments and simulations become increasingly relevant in combustion, it is essential that conventions and best practices are established for the field, to prevent confusion, error, and miscommunication between researchers. In this section, we describe the influence of real gas behavior on mass-action kinetics. The rate of progress (ROP,  $\dot{q}$ ) for a reversible reaction is written according to mass-action kinetics as [50, 51]:

$$\dot{q} = \frac{1}{\gamma^*} \left( k_f \prod C_{\text{ac},k}^{\nu_k'} - k_r \prod C_{\text{ac},k}^{\nu_k''} \right), \quad (19)$$

where  $\nu_k'$  and  $\nu_k''$  are the forward and reverse stoichiometric coefficients for species  $k$ , respectively,  $k_f$  and  $k_r$  are the forward and reverse rate constants,  $\gamma^*$  is the activity coefficient of the activated complex in the transition state, and  $C_{\text{ac},k}$  is the activity concentration of species  $k$ :

$$C_{\text{ac},k} = \alpha_k [X_k^\circ], \quad (20)$$

where  $\alpha_k$  is the species activity and  $[X_k^\circ]$  is the species molar concentration ( $\text{mol}_k \text{ m}^{-3}$ ) for the adopted thermodynamic reference state  $p^\circ X_k R^{-1} T^{-1}$ , for the current work). Using the activity coefficient  $\gamma_k$ , we arrive at:

$$C_{\text{ac},k} = \gamma_k [X_k], \quad (21)$$

Note that this can be converted into a number of equivalent forms to represent departure from ideality (such as the species fugacity  $f_k$ ). For example, the molar concentration can be written as:

$$[X_k] = \frac{p X_k}{ZRT}, \quad (22)$$

which results in

$$C_{\text{ac},k} = \frac{\gamma_k p X_k}{ZRT}. \quad (23)$$

For an ideal gas,  $Z = 1$  and  $\gamma_k = 1$ , such that:

$$C_{\text{ac},k, \text{Ideal gas}} = \frac{p X_k}{RT}. \quad (24)$$

The concept of the activity concentration is an oft-neglected aspect of mass-action kinetics, as many studies adopt some form of the ideal gas standard, setting  $\gamma_k$  and/or  $Z$  equal to 1. Correctly calculating the activity concentrations is more than an academic point: the form used for  $C_{\text{ac},k}$  in the law of mass-action determines how the kinetic parameters  $k_f$  are fit to experimental data for a given set of reactions. As  $C_{\text{ac},k}$  depends explicitly on the adopted thermodynamic reference state (c.f. Eq. 20), reference states must be communicated clearly so they can be readily implemented by any researchers adopting a given reaction mechanism.

Real gas effects on the forward rate constant  $k_f$  can be calculated assuming equilibrium with the activated complex:

$$k_f = k^\circ K_{\text{eq,TS}}, \quad (25)$$

where  $k^\circ$  is a function of temperature only and can be related to the vibrational energy mode that allows dissociation of the activated complex. As described by Froment and Bischoff,  $k^\circ$  can be calculated from statistical mechanics [50].  $K_{\text{eq,TS}}$  is the equilibrium constant between the reactants and the transition state:

$$K_{\text{eq,TS}} = \frac{\gamma^* [X^*]}{\prod_k (\gamma_k [X_k])^{\nu_k'}}, \quad (26)$$

where  $[X^*]$  is the molar concentration of the transition state complex. Similar arguments for  $k_r$ , plus the assumption of microscopic thermodynamic reversibility, lead to:

$$k_r = \frac{k_f}{K_{\text{eq}}}, \quad (27)$$

where  $K_{\text{eq}}$  is the reaction equilibrium coefficient, defined according to the reference-state species thermodynamics and a function of temperature only. The rate constants may incorporate real gas effects (Eqs. 25 and 26), but the ratio between  $k_f$  and  $k_r$  is not affected by non-ideality. A derivation for a real gas  $K_{\text{eq}}$  is given in the Supplementary Information.

As described previously, dividing by  $\gamma^*$  in Eq. 19 is required because the reaction rate is proportional to the *concentration* of the transition state, not its activity concentration [50]. Tang and Brezinsky outline possible methods for calculating  $\gamma^*$  [23], but note that the calculation is currently infeasible for large-scale simulations. As in that work,  $\gamma^* = 1$  is assumed, here.

### 3.2.2. Real gas activities: Redlich–Kwong EoS

As established, the activity coefficient is assumed to be unity for an ideal gas. For a real gas, the activities and activity coefficients are derived directly from the EoS. The species activity is defined as proportional to the departure of the species chemical potential  $\mu_k$  from that of the adopted reference state,  $\mu_k^\circ$ :

$$\alpha_k = \exp\left(\frac{\mu_k - \mu_k^\circ}{RT}\right). \quad (28)$$

The chemical potential departure function  $\mu_k - \mu_k^\circ$  can be defined relative to the Helmholtz departure function:

$$\mu_k - \mu_k^\circ = \left(\frac{\partial(n_T a - n_T a^\circ)}{\partial n_k}\right)_{T, V, n_{j \neq k}}, \quad (29)$$

where  $n_T$  is the total number of moles and with the differentiation carried out at constant temperature, constant volume, and constant number of moles for all species other than  $k$ . In short, combining Eq. 29 with Eq. 18 gives the following for the chemical potential departure function:

$$\begin{aligned} \mu_k - \mu_k^\circ = & -RT \ln\left(\frac{p^\circ (v - b_{\text{mix}}^*)}{RT}\right) + RT \left(\frac{b_k^*}{v - b_{\text{mix}}^*}\right) \\ & + \frac{a_{\text{mix}}^* b_k^* - 2b_{\text{mix}}^* \sum_j a_{jk}^* X_j}{b_{\text{mix}}^{*2} \sqrt{T}} \ln\left(\frac{v + b_{\text{mix}}^*}{v}\right) \\ & - \frac{a_{\text{mix}}^*}{b_{\text{mix}}^* \sqrt{T}} \left(\frac{b_k^*}{v + b_{\text{mix}}^*}\right). \end{aligned} \quad (30)$$

Combined with Eqs. 28 and 21, and keeping in mind the adopted reference state ( $[X_k^\circ] = p^\circ X_k/RT$ ), the activity coefficient  $\gamma_k$  can therefore be calculated via:

$$\begin{aligned} RT \ln(\gamma_k) = & RT \ln\left(\frac{v}{v - b_{\text{mix}}^*}\right) + RT \left(\frac{b_k^*}{v - b_{\text{mix}}^*}\right) \\ & + \frac{a_{\text{mix}}^* b_k^* - 2b_{\text{mix}}^* \sum_j a_{jk}^* X_j}{b_{\text{mix}}^{*2} \sqrt{T}} \ln\left(\frac{v + b_{\text{mix}}^*}{v}\right) \\ & - \frac{a_{\text{mix}}^*}{b_{\text{mix}}^* \sqrt{T}} \left(\frac{b_k^*}{v + b_{\text{mix}}^*}\right). \end{aligned} \quad (31)$$

The derivation of Eq. 31 is described in greater detail in the Appendix.

## 4. Experimental Shock Tube Results

Measured ignition delay times for n-dodecane are shown in Fig. 2. For the present conditions, the ignition delay times span 65 to 434  $\mu\text{s}$  and illustrate NTC behavior with a transition from low-temperature to NTC behavior around 850 K and a transition from NTC to high-temperature behavior around 1000 K. The IDTs decrease with increasing pressure across the entire temperature domain but with stronger pressure dependence in the NTC region than at high temperatures. IDTs for  $\phi=2$  mixtures are approximately 50% shorter than for  $\phi=1$ . Reduced  $\text{O}_2$  concentration mixtures show increased IDTs with decreasing  $\text{O}_2$  concentration, with increased dependence on  $\text{O}_2$  concentration for NTC temperatures, relative to high temperatures.

While there are no data available within the literature to directly compare with the present results, the data are compared in Fig. 3 to shock tube IDT measurements for n-dodecane at  $p = 20$  atm by Vasu et al. [9] and with results for n-decane reported at 50 atm by Pfahl et al. [12] and 80 atm by Zhukov et al. [13]. All the data exhibit similar temperature dependence and at high pressures the n-decane and n-dodecane results are in agreement within the experimental scatter/uncertainty, as expected based on the similarity of IDTs for large n-alkanes.

## 5. Modeling Results

### 5.1. Verification against CHEMKIN simulation results

Before comparing simulation results with experimental data, the accuracy of the constant volume, adiabatic reactor code is first verified against the commercial CHEMKIN code.<sup>2</sup> Both the codes are run with the

<sup>2</sup>ANSYS, Inc; Canonsburg, PA, USA; [www.ansys.com](http://www.ansys.com)

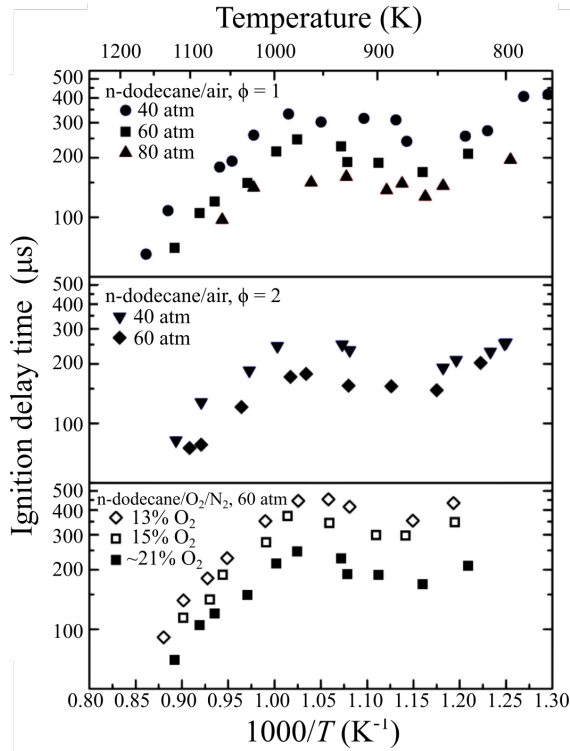


Figure 2: Ignition delay measurements for n-dodecane.

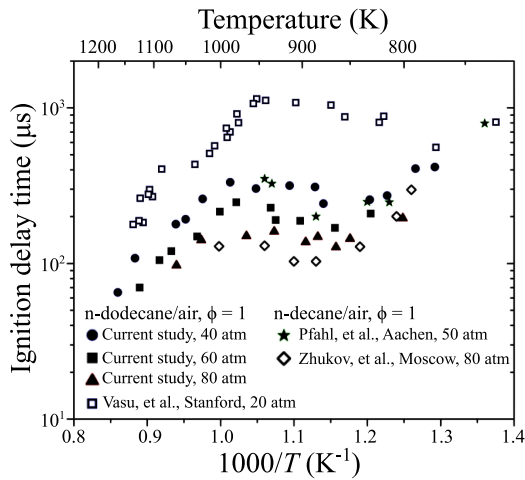


Figure 3: Comparison of present ignition delay measurements for stoichiometric n-dodecane/air to previous measurements for n-dodecane [9] and n-decane [12, 13] from the literature.

ideal gas EoS, at pressures of 40, 60, and 80 atm, and the pressure and temperature histories are compared. As shown in Fig. 4, pressure and temperature histories from the model used in this study (with properties calculated via CANTERA) match exactly with those from CHEMKIN.

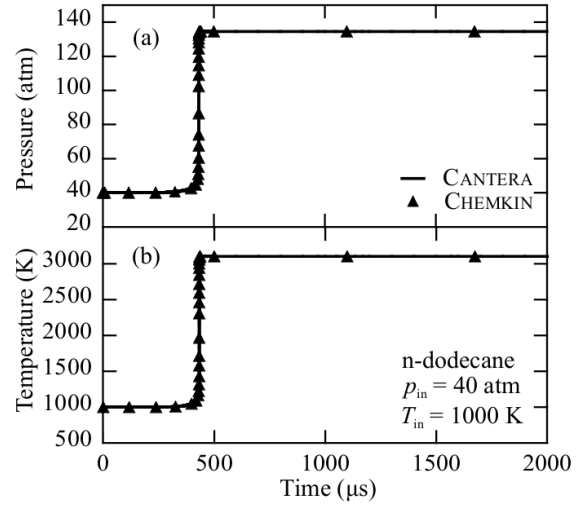


Figure 4: Comparison of (a) pressure and (b) temperature histories for simulations carried out using CHEMKIN and CANTERA.

## 5.2. Non-ideal effects on ignition delay times

The shock tube experiments at Rensselaer Polytechnic Institute were performed for stoichiometric and rich n-dodecane/air mixtures at 40, 60, and 80 atm. Simulations at  $\phi=2.0$  yielded no new insights regarding real gas effects, relative to those at  $\phi=1.0$ ; as such, simulation results are only presented for  $\phi=1.0$ . In the present study, we examine the extent of non-ideality in predicted IDTs via three different thermodynamic and chemical kinetic implementations:

### 1. Ideal gas thermodynamics and kinetics:

The ideal gas EoS (Eq. 4) is used for  $p$ ,  $T$ ,  $v$ , and thermodynamic calculations, and  $\gamma_k=1$  is assumed for all species (i.e., Eq. 24 is used for the activity concentrations in Eq. 19). Results are labeled ‘Ideal gas’ in the subsequent figures.

### 2. Real gas thermodynamics, ideal gas kinetics:

The R–K EoS (Eq. 6) and associated derivations (Eqs. 18, 30, etc.) are used for  $p$ ,  $T$ ,  $v$ , and thermodynamic calculations, but the chemical kinetic calculations assume an activity coefficient of unity for all species (i.e., the species activity concentration is replaced by the species concentration,  $C_{ac,k} = [X_k]$ ). Results for this implementation are labeled ‘R–K ( $[X_k]$ )’.

### 3. Real gas thermodynamics and kinetics:

The R–K EoS (Eq. 6) and associated derivations (Eqs. 18, 30, etc.) are used for  $p$ ,  $T$ ,  $v$ , and thermodynamic calculations, and activity coefficients  $\gamma_k$  are calculated via Eq. 31. Results for this implementation are labeled ‘R–K ( $\gamma_k$ )’.

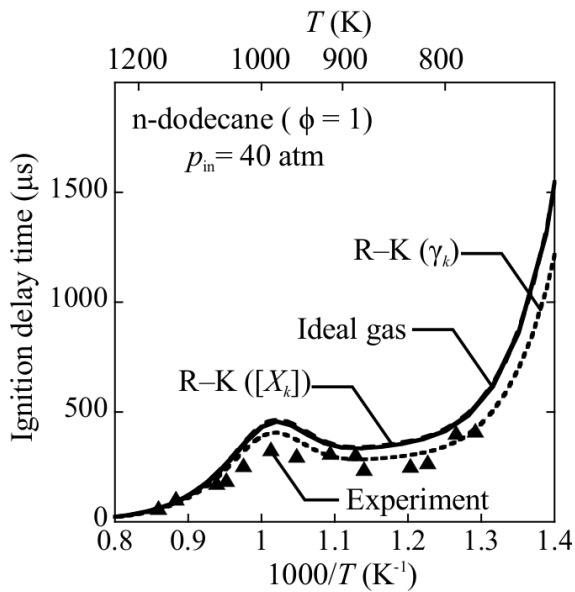


Figure 5: Ignition delay time as a function of temperature for different EoS at 40 atm.

Note that the ‘R–K ( $[X_k]$ )’ model is not thermodynamically consistent. The species concentrations  $[X_k]$  is calculated as  $(X_k/\nu)$ , according to the actual EoS (Eq. 6), whereas the activity concentrations are calculated using  $\gamma_k=1$ . However, in the absence of clearly established best practices for such calculations, it is an implementation that might reasonably be applied by researchers to incorporate real gas effects. The implications of such an implementation are therefore worth considering.

Figure 5 shows predicted IDTs as a function of temperature for all three models at 40 atm, along with the experimental shock tube data. IDTs for all three models correctly match qualitative trends, including convergence toward  $IDT = 0 \mu s$  for  $T > 1050 \text{ K}$ , NTC behavior

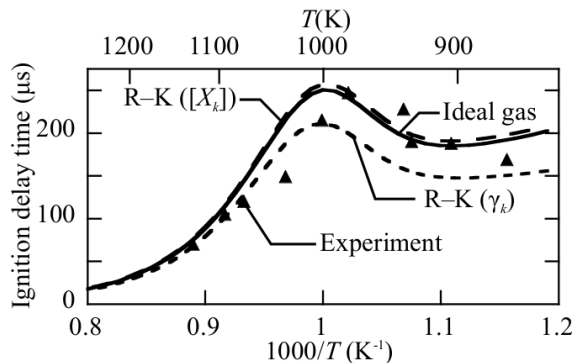


Figure 6: Ignition delay time as a function of temperature in the NTC and high-temperature regions at 60 atm.

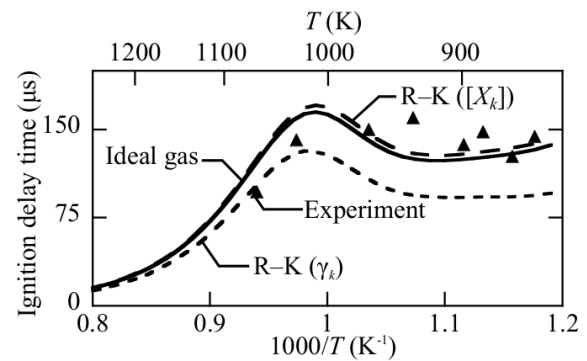


Figure 7: Ignition delay time as a function of temperature in the NTC and high-temperature regions at 80 atm.

at intermediate temperatures, and a sharp increase toward very high IDTs at low temperature. At 40 atm, the R–K EoS with activity coefficients predicts the experimental data most accurately. Figures 6 and 7 show similar comparisons at 60 atm and 80 atm, respectively, and focus on the NTC and high-temperature regions. Here, it is difficult to conclude the accuracy of any one EoS, as all plots lie within the relative uncertainty of the experiments, which is estimated at  $\pm 20\%$ . Regardless, the real gas effect is approximately  $50 \mu s$  in the NTC at all three pressures, which is similar in magnitude to the experimentally-measured NTC effect. The relative IDT change due to real gas effects in the NTC region is approximately 10% at 40 atm., and increases to  $> 30\%$  at 80 atm. As expected, real gas effects become prominent with decreasing temperature (approximately  $T < 1000$ ), as fuel species approach their critical properties, and are insignificant for  $T > 1000 \text{ K}$  (i.e.,  $(1/T) < 1.0$ )

Comparing the two real gas implementations (i.e., ‘R–K ( $[X_k]$ )’ and ‘R–K ( $\gamma_k$ )’), implementing only the R–K EoS without also considering activity coefficients (i.e., the ‘R–K ( $[X_k]$ )’ model) implies that real gas effects have minimal importance at these conditions. While the thermodynamically consistent ‘R–K ( $\gamma_k$ )’ model predicts IDTs lower than the ideal gas case, the ‘R–K ( $[X_k]$ )’ model predicts a very slight increase in IDTs, due to real gas effects. Great care must therefore be taken to develop thermodynamically consistent EoS implementations, particularly as it relates to species activity concentrations for mass-action kinetics.

The differences between the three thermo-kinetic models are readily explained by considering the mixture compressibility  $Z$  and the species activity coefficients  $\gamma_k$ . Because the trends in Figs. 5–7 do not vary strongly as a function of pressure, subsequent analysis focuses on a single illustrative case,  $p_{in} = 40 \text{ atm}$ . For the ‘R–K

( $[X_k]$ )' model, the real gas effect is captured entirely by the compressibility  $Z$  and Eq. 23. As discussed below, the high concentration of  $N_2$  means that the mixture behaves essentially as an ideal gas. For  $p_{in} = 40$  atm and  $T_{in} = 1000$  K,  $Z$  ranges from 1.01–1.02, as in Figure 8, and hence the molar concentrations are  $1.02^{-1}$ – $1.01^{-1}$  times those of an ideal gas at the same  $T$  and  $p$ . From Eq. 19 and 23, the predicted IDTs for the ideal gas and 'R–K ( $[X_k]$ )' models therefore scale very closely with the compressibility: the 'R–K ( $[X_k]$ )' IDT is 1.015 times that of the ideal gas simulation, at  $p_{in} = 40$  atm and  $T_{in} = 1000$  K. For the 'R–K ( $\gamma_k$ )' implementation, the activity concentrations are scaled by both  $Z$  and  $\gamma_k$ , as per Eq. 22. While the compressibility suppresses the activity concentrations very slightly, as in the 'R–K ( $[X_k]$ )' case, the activity coefficients are  $> 1$  for the major reactants, as shown in Figure 9. The increased  $\gamma_k$  values dominate over the small increase in  $Z$ , leading to higher activity concentrations and therefore lower IDTs in the 'R–K ( $\gamma_k$ )' model.

This analysis also helps explain predictions by Tang and Brezinsky [23], who similarly separate the real gas effects into ' $p-v-T$ ' and 'kinetic rate parameter' components (as well as an enthalpy effect, which they conclude is insignificant). They consider real gas effects on ethylene profiles at 605 atm, and similarly find that the  $p-v-T$  and kinetic components affect the reaction rates in opposite ways. The methodologies are slightly different in the two studies: Tang and Brezinsky look at real gas effects on the reverse rate constant  $k_r$ , whereas our approach has a constant  $k_r$ , as shown in the Supplementary Information, but varies how the activity concentration is calculated for real gases. Regardless, Tang and Brezinsky's findings are consistent with the preceding discussion of how  $Z$  and  $\gamma_k$  influence combustion properties. Furthermore, the larger  $p-v-T$  effect in the Tang and Brezinsky results, compared to the insignificant effect in the 'R–K ( $[X_k]$ )' model here, is consis-

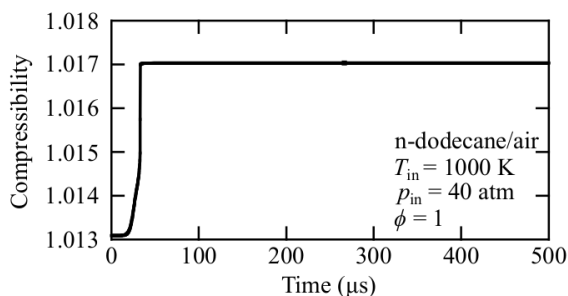


Figure 8: Compressibility as a function of time for n-dodecane/air at  $T_{in} = 1000$  K,  $p_{in} = 40$  atm, and  $\phi = 1$ .

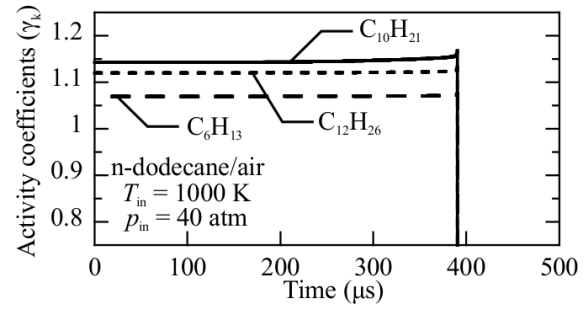


Figure 9: Activity coefficients as a function of time for selected species for  $T_{in} = 1000$  K and  $p_{in} = 40$  atm.

tent with our analysis, given the higher pressure considered, there: the R–K EoS predicts  $Z = 1.14$  at the conditions explored by Tang and Brezinsky, compared to  $1.01 \leq Z \leq 1.02$  in our study.

While real gas effects influence IDTs at these conditions, they are moderated by effect of the bath gas. Simulations here assume a stoichiometric mixture of air and n-dodecane, and hence the  $N_2$  mole fraction is 78.1%. Therefore, the  $N_2$  compressibility ( $\approx 1.0$ , as in Table 2) largely dictates the average mixture compressibility. Figure 8 shows the temporal evolution of the mixture compressibility during combustion, for  $p_{in} = 40$  atm and  $T_{in} = 1000$  K. Although the initial compressibility of the fuel ( $C_{12}H_{26}$ ) is 0.85, the average compressibility of the mixture remains near unity during the entire simulation. Even with varying equivalence ratio, as in Fig. 10, the  $N_2$  bath gas keeps the initial mixture near the ideal gas regime. Rather than the mixture compressibility, the individual reacting species' compressibilities and activity coefficients must be considered, when predicting real gas effects in combustion applications. Furthermore, real gas effects at supercritical pressures may be even more significant in applications such as oxy-combustion or fuel pyrolysis, where combustion

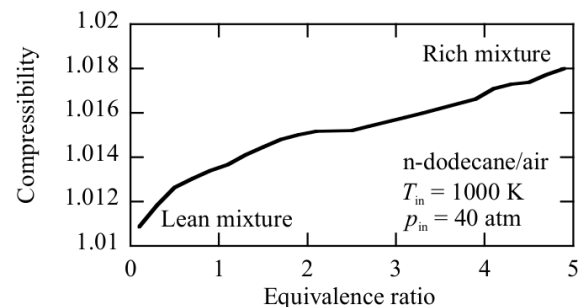


Figure 10: Compressibility as a function of equivalence ratio at 40 atm.

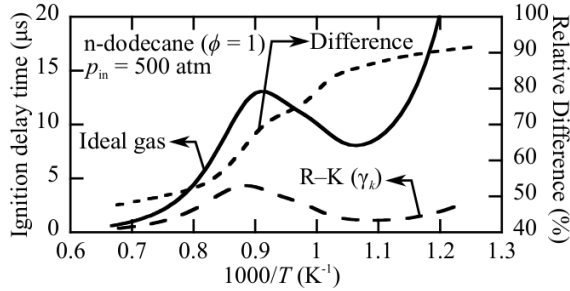


Figure 11: Ignition delay time as a function of temperature at 500 atm.

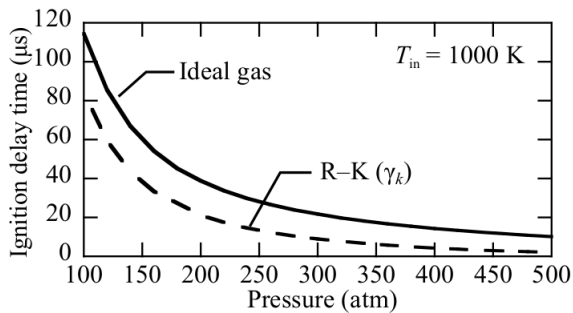


Figure 12: Comparison of ignition delay time at high pressures.

occurs without any bath gas [52–56]. While beyond the scope of this work, additional study is required to determine the impact of non-idealities at elevated pressures in such applications.

The moderating influence of the bath gas is further illustrated by considering ignition at very high pressures (500 atm), where the fuel and bath gas are both supercritical, with  $Z > 1.1$  for all temperatures explored above. Fig. 11 shows predicted IDTs for the ‘Ideal gas’ and ‘R–K ( $\gamma_k$ )’ models. The relative difference between the IDTs is  $> 40\%$ , for all temperatures investigated. This difference is even higher ( $> 70\%$ ) near the NTC region. Finally, real gas effects at a range of elevated pressure are summarized in Fig. 12, which shows predicted IDTs for the ideal gas and R–K EoS for  $100 \text{ atm} \leq p \leq 500 \text{ atm}$ , with  $T_{\text{in}} = 1000 \text{ K}$ . Consistent with Figs. 5–7, the difference between the two EoS ranges from 20 to  $50 \mu\text{s}$  at all pressures. For  $p \geq 175 \text{ atm}$ , the overall decrease in IDTs results in predicted ideal gas IDTs that are 2 to 3 times higher than via the R–K EoS. Although IDTs at such pressures have not been reported in the literature, these results motivate additional study of real gas effects at very high pressures, and demonstrate how the compressibility of the bath gas at pressures  $< 100 \text{ atm}$  significantly moderate the influence of real gas effects.

Table 3: Sensitive reactions for formation of  $\text{CO}_2$ ,  $\text{H}_2\text{O}$ .

#	Reaction
1	$2 \text{ OH} + \text{M} \leftrightarrow \text{H}_2\text{O}_2 + \text{M}$
2	$\text{CH}_3 + \text{HO}_2 \leftrightarrow \text{CH}_3\text{O} + \text{OH}$
3	$\text{C}_2\text{H}_4 + \text{OH} \leftrightarrow \text{C}_2\text{H}_3 + \text{H}_2\text{O}$
4	$\text{C}_{12}\text{H}_{26} + \text{HO}_2 \leftrightarrow \text{C}_{12}\text{H}_{25} + \text{H}_2\text{O}_2$
5	$\text{C}_6\text{H}_{13} \leftrightarrow \text{C}_3\text{H}_6 + \text{C}_3\text{H}_7$
6	$\text{C}_6\text{H}_{12}\text{OOHO}_2 \leftrightarrow \text{C}_6\text{H}_{12}\text{O}_3 + \text{OH}$
7	$\text{H}_2\text{O}_2 + \text{O}_2 \leftrightarrow 2 \text{ H}_2\text{O}$
8	$\text{C}_6\text{H}_{12}\text{OOH} \leftrightarrow \text{C}_6\text{H}_{12}\text{O} + \text{OH}$
9	$\text{C}_4\text{H}_9 \leftrightarrow \text{C}_3\text{H}_6 + \text{CH}_3$
10	$\text{C}_{12}\text{H}_{26} + \text{O}_2 \leftrightarrow \text{C}_{12}\text{H}_{25} + \text{HO}_2$

### 5.3. Chemical kinetics and sensitivity analysis

It is important to acknowledge the significant influence of the adopted thermo-kinetic mechanism on model-predicted IDTs. Typically, reaction mechanisms are developed and validated under ideal-gas assumptions, but are expected to be applied to different reactor systems with varying pressures and temperatures. The effect of pressure can be introduced via ‘pressure dependent’ reactions using Chebyshev representations, but because rate expressions also include the concentration and activity dependencies of individual species, a kinetic mechanism’s accuracy may vary across a wide range of non-ideal conditions.

While the net ROPs may therefore be inaccurate depending on the EoS used, detailed reaction mechanisms frequently contain thousands of reactions steps among hundreds of species. The difference in net production rates with varying EoS may not be important for all species and all reaction steps. For the given n-dodecane mechanism, a sensitivity analysis was therefore performed using CHEMKIN software, to determine key rate-limiting reactions. For these key reactions, listed in Table 3, we then compared rates of progress between the ‘Ideal gas’ and ‘R–K ( $\gamma_k$ )’ implementations. All results presented in this section were calculated at the time of ignition, with initial conditions  $T=1000 \text{ K}$  and  $p=40 \text{ atm}$ .

As seen in Table 3, reactions containing higher carbon compounds and certain Hydrogen compounds ( $\text{H}_2\text{O}$ ,  $\text{H}_2\text{O}_2$ ,  $\text{OH}$ ,  $\text{HO}_2$ ) are important for accurate IDT predictions. Among these, the largest absolute differences in the net production rates between the three thermo-kinetic implementations are observed for reactions 1–3, as shown in Figure 13. For all three reactions, the ‘R–K ( $\gamma_k$ )’ rates of progress have larger magnitudes than those from the ideal gas implementation.

Figure 14 shows relative ROP differences between

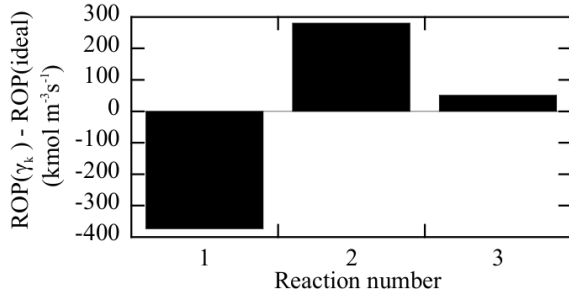


Figure 13: Absolute net ROP differences for selected reactions between ideal gas and R-K ( $\gamma_k$ ) models, at the time of ignition.  $T_{in} = 1000$  K,  $p_{in} = 40$  atm.

the ‘Ideal gas’ and ‘R-K( $\gamma_k$ )’ implementations, calculated as:

$$\Delta ROP_{rel}(\%) = 100 \times \left| \frac{ROP_{ideal} - ROP_{real}}{ROP_{ideal}} \right|. \quad (32)$$

Although reactions 1–3 show significant absolute differences in ROP for three implementations, these same reactions have comparatively small relative differences. Instead, reactions 4 and 10, which contain n-dodecane fuel, show the largest relative differences. This is expected, since n-dodecane is non-ideal ( $Z \neq 1$ ) at the given operating conditions, leading to differences in the n-dodecane activity concentration between the ideal gas and R-K EoS.

In addition to the highly sensitive reactions in Table 3, if progress rates for all 432 reactions are compared, reactions with higher hydrocarbons and aromatic compounds have the largest  $\Delta ROP_{rel}$  values. Some of these reactions are listed in Table 4, and  $\Delta ROP_{rel}$  values are shown in Fig. 15. The compressibilities for major species in these reactions are plotted in Fig. 16, and show significant departure from  $Z = 1$  during combustion. While real gas effects are therefore more significant for the reactions in Table 4 than for those in Table 3, the mole fractions of the intermediate species

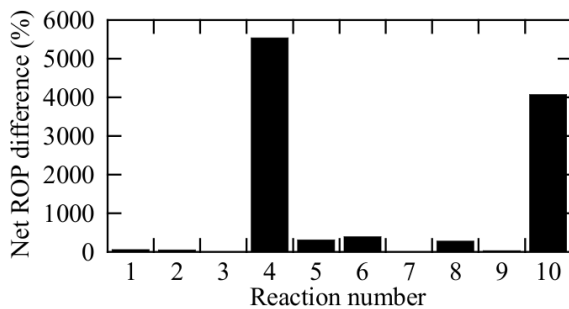


Figure 14: Relative differences between net ROP of ideal gas model and R-K model, at the time of ignition.  $T_{in} = 1000$  K,  $p_{in} = 40$  atm.

Table 4: Reactions exhibiting on maximum relative difference in ROP.

#	Reaction
11	$C_4H_5 + C_2H \leftrightarrow C_6H_6$
12	$C_{12}H_{25} + HO_2 \rightarrow C_{12}H_{26} + H_2O_2$
13	$C_{12}H_{26} + H_2O_2 \rightarrow C_{12}H_{25} + HO_2$
14	$C_{12}H_{25} + HO_2 \leftrightarrow C_{12}H_{26} + O_2$
15	$C_{12}H_{25}O_2 + O_2 \leftrightarrow C_{12}H_{24}O_3 + OH$
16	$C_{12}H_{26} + CH_3 \rightarrow C_{12}H_{25} + CH_4$
17	$C_{12}H_{25} + CH_4 \rightarrow C_{12}H_{26} + CH_3$
18	$C_{10}H_{21}O_2 + O_2 \leftrightarrow C_{10}H_{20}O_3 + OH$
19	$C_{10}H_{20}O_3 \rightarrow OH + CH_3CO + C_{17}H_{15}CHO$
20	$C_{10}H_{20}O_3 \rightarrow OH + C_2H_5CO + C_6H_{13}CHO$

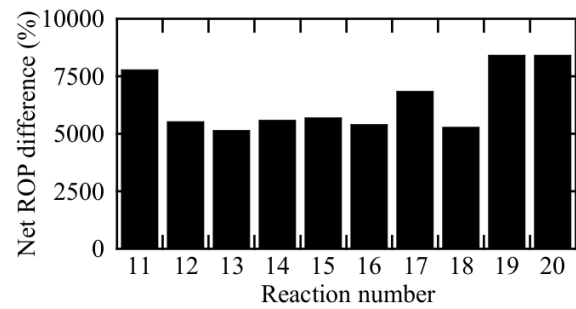


Figure 15: Relative differences between net ROP of ideal gas model and R-K model, at the time of ignition.  $T_{in} = 1000$  K,  $p_{in} = 40$  atm.

in Fig. 16 are very small, and as such these species don’t have a significant impact on the overall mixture compressibility. This implies that, although not specifically considered here, real gas effects should be more significant for chemical processes in which molecular weight growth is important (e.g., hydrocarbon pyrolysis reactions). Regardless, these results demonstrate that non-ideal behavior for species participating in key rate-limiting reaction steps can have a significant impact on combustion dynamics, regardless of the average mixture compressibility.

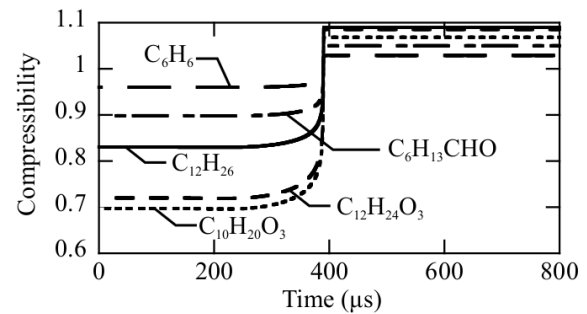


Figure 16: Individual compressibilities of few intermediate species.  $T_{in} = 1000$  K,  $p_{in} = 40$  atm.

## 6. Conclusions

The objective of this research article is to explore possible non-idealities introduced in high-pressure shock tube reactors and demonstrate the magnitude of their effects on ignition characteristics. A shock tube reactor, when operated at trans-critical and supercritical pressures, shows real gas effects on ignition delay and NTC regions, primarily due to the impact of non-idealities on species activities and their subsequent impact on chemical reaction rates. Many intermediate, short-lived species during combustion, especially higher carbon number and cyclic compounds, deviate significantly from ideal gas behavior. While the contribution of these species to the average compressibility of the mixture is very low, due to the high mole fraction of the bath gas, the departure from ideal behavior for these species has a significant effect on the ignition characteristics. These results demonstrate that the average mixture compressibility is not a sufficient metric for evaluating the importance of real gas effects in combustion applications.

Shock tube simulations are compared to new ignition delay time measurements for n-dodecane performed at ( $40 \text{ atm} < p < 80 \text{ atm}$ ) and for temperatures ( $774 \text{ K} < T < 1163 \text{ K}$ ) spanning the low-temperature, NTC, and high-temperature regimes. These measurements are the first data for n-dodecane carried out at the very high pressures found in compression-ignition engines and next-generation gas turbines.

Under the operating conditions studied here, incorporating non-idealities decreases the predicted ignition times by approximately 20% between the R–K and ideal gas EoS simulations at a pressure of 40 atm. Although the non-ideal effects are moderate at 40 atm, they increase in significance at elevated operating pressures. At  $p=80 \text{ atm}$ , the relative difference between ideal and real gas EoS predicted ignition delay times is roughly 50% in the NTC region. Moreover, this study highlights the fact that the chemical reaction rates should be expressed in a thermodynamically consistent manner. In other words, activity concentration expressions should be derived from the thermodynamic EoS, rather than adopting the ideal gas convention (i.e., using molar concentration as a stand-in for the activity concentration).

Finally, it is imperative that real gas effects are considered during the development of new kinetic mechanisms. For key intermediate species present at low relative concentrations, net production rates may vary significantly between ideal and real gas EoS. Hence, the applicability of these kinetic reaction mechanisms rely

on choosing a suitable equation of state to determine the rate constants and their temperature and pressure dependencies.

## 7. Acknowledgements

This work was supported by the Air Force Office of Scientific Research, under grants #FA9550-16-1-0349 (CSM), and #FA9550-11-1-0261 (RPI), Program Manager: Dr. Chiping Li. We gratefully acknowledge insightful discussions with Dr. Harry Moffatt, Prof. Greg Jackson, and Dr. Huayang Zhu.

## References

- [1] O. Redlich, J. Kwong, On the thermodynamics of solutions. V. An equation of state. Fugacities of gaseous solutions, *Chem. Rev.* 44 (1949) 233–244.
- [2] G. Soave, Equilibrium constants from a modified Redlich–Kwong equation of state., *Chem. Eng. Sci.* 27 (1972) 1197–1203.
- [3] D. Peng, D. Robinson, A new two-constant equation of state., *Ind. Eng. Chem. Fund.* 15 (1976) 59–64.
- [4] L. Pickett, Engine Combustion Network Data Archive, <http://www.sandia.gov/ecn/index.php> (2016).
- [5] L. Pickett, C. Genzale, G. Bruneaux, L. Malbec, L. Hermant, C. Christiansen, J. Schramm, Comparison of diesel spray combustion in different high-temperature, high-pressure facilities, *SAE Int. J. Eng.* 3 (2010) 156–181.
- [6] L. Pickett, J. Manin, C. Genzale, D. Siebers, M. Musculus, C. Idicheria, Relationship between diesel fuel spray vapor penetration/dispersion and local fuel mixture fraction, *SAE Int. J. Eng.* 4 (2001) 764–799.
- [7] R. Payri, J. G.-O. M. Bardi, J. Manin, Fuel temperature influence on diesel sprays in inert and reacting conditions, *Appl. Therm. Eng.* 35 (2012) 185–195.
- [8] D. Davidson, D. Haylett, R. Hanson, Development of an aerosol shock tube for kinetic studies of low-vapor-pressure fuels, *Combust. Flame* 155 (2008) 108–117.
- [9] S. Vasu, D. Davidson, Z. Hong, V. Vasudevan, R. Hanson, n-Dodecane oxidation at high-pressures: Measurements of ignition delay times and OH concentration time-histories, *Proc. Combust. Inst.* 32 (2009) 173–180.
- [10] H. Shen, J. Steinberg, J. Vanderover, M. Oehlschlaeger, A shock tube study of the ignition of n-Heptane, n-Decane, n-Dodecane, and n-Tetradecane at elevated pressures, *Energ. Fuel* 23 (2009) 2482–2489.
- [11] D. Haylett, D. Davidson, R. Hanson, Ignition delay times of low-vapor-pressure fuels measured using an aerosol shock tube, *Combust. Flame* 159 (2012) 552–561.
- [12] U. Pfahl, K. Fieweger, G. Adomeit, Self-ignition of diesel-relevant hydrocarbon-air mixtures under engine conditions, *Proc. Combust. Inst.* 26 (1996) 781–789.
- [13] V. Zhukov, V. Sechenov, A. Starikovskii, Autoignition of n-decane at high pressure, *Combust. Flame* 153 (2008) 130–136.
- [14] K. Kumar, G. Mittal, C. Sung, Autoignition of n-decane under elevated pressure and low-to-intermediate temperature conditions, *Combust. Flame* 156 (2009) 1278–1288.
- [15] E. Petersen, R. Hanson, Nonideal effects behind reflected shock waves in a high-pressure shock tube, *Shock Waves* 10 (2001) 405–420.

- [16] Z. Hong, G. Pang, S.S.Vasu, D. Davidson, R. Hanson, The use of driver inserts to reduce non-ideal pressure variations behind reflected shock waves., *Shock Waves* 19 (2009) 113–123.
- [17] H. Li, Z. Owens, D. Davidson, R. Hanson, A simple reactive gasdynamic model for the computation of gas temperature and species concentrations behind reflected shock waves, *Int. J. Chem. Kinet.* 40 (2008) 189–198.
- [18] R. Sivaramakrishnan, A. Comandini, R. Tranter, K. Brezinsky, S. Davis, H. Wang, Combustion of CO/H<sub>2</sub> mixtures at elevated pressures., *Proc. Comb. Inst.* 31 (2007) 429–437.
- [19] D. Davidson, R. Hanson, Real gas corrections in shock tube studies at high pressures., *Israel J. Chem.* 36 (1996) 321–326.
- [20] R.G.Schmitt, P.B.Butler, N.B.French, Chemkin Real Gas: A Fortran Package for Analysis of Thermodynamic Properties and Chemical Kinetics in Nonideal Systems, Iowa City : University of Iowa, 1994.
- [21] R. Kee, F. Rupley, J. Miller, Chemkin-II: a Fortran chemical kinetics package for the analysis of gas phase chemical kinetics., Technical Report SAND89-8009, Sandia National Laboratories.
- [22] R.G.Schmitt, P.B.Butler, Detonation properties of gases at elevated initial pressures, *Combust. Sci. Technol.* 106 (1995) 167–191.
- [23] W. Tang, K. Brezinsky, Chemical kinetic simulations behind reflected shock waves, *Int. J. Chem. Kinet.* 38 (2006) 75–97.
- [24] E. Petersen, D. Davidson, R. Hanson, Kinetics modeling of shock-induced ignition in low-dilution CH<sub>4</sub>/O<sub>2</sub> mixtures at high pressures and intermediate temperatures, *COMBUSTION AND FLAME* 117 (1-2) (1999) 272–290. doi:[10.1016/S0010-2180\(98\)00111-4](https://doi.org/10.1016/S0010-2180(98)00111-4).
- [25] CHEMKIN-PRO, ANSYS, Inc; Canonsburg, PA, USA.
- [26] R. Tranter, R. Sivaramakrishnan, K. Brezinsky, M. Allendorf, High pressure, high temperature shock tube studies of ethane pyrolysis and oxidation, *Phys. Chem. Chem. Phys.* 4 (2002) 2001–2010.
- [27] H. Wang, M. Oehlschlaeger, Autoignition studies of conventional and Fischer–Tropsch jet fuels, *Fuel* 98 (2012) 249–258.
- [28] X. Fu, S. Aggarwal, Two-stage ignition and NTC phenomenon in diesel engines., *Fuel* 144 (2015) 188–196.
- [29] B. Koroglu, O. Pryor, J. Lopez, L. Nash, S. Vasu, Shock tube ignition delay times and methane time-histories measurements during excess CO<sub>2</sub> diluted oxy-methane combustion., *Combust. Flame* 164 (2016) 152–163.
- [30] C. Barraza-Botet, S. Wagnon, M. Wooldridge, Combustion chemistry of ethanol: Ignition and speciation studies in a rapid compression facility., *J. Phys. Chem. A* 120 (2016) 7408–7418.
- [31] D. Goodwin, H. Moffat, R. Speth, Cantera: An object-oriented software toolkit for chemical kinetics, thermodynamics, and transport processes, <http://www.cantera.org> (2017). doi:[10.5281/zenodo.170284](https://doi.org/10.5281/zenodo.170284).
- [32] L. Shampine, M. Reichelt, The MATLAB ODE suite., *SIAM J. Sci. Comput.* 18 (1997) 1–22.
- [33] H. Wang, Y. Ra, M. Jia, R. Reitz, Development of a reduced n-dodecane-PAH mechanism. and its application for n-dodecane soot predictions., *Fuel* 136 (2014) 25–36.
- [34] H. Shen, M. Oehlschlaeger, The autoignition of C<sub>8</sub>H<sub>10</sub> aromatics at moderate temperatures and elevated pressures, *Combust. Flame* 156 (2009) 1053–1062.
- [35] W. Wang, S. Gowdagiri, M. Oehlschlaeger, The high-temperature autoignition of biodiesels and biodiesel components, *Combust. Flame* 161 (2014) 3014–3021.
- [36] J. V. der Waals, On the continuity of the gaseous and liquid states, PhD dissertation, Universiteit Leiden (1873).
- [37] R. Aungier, A fast, accurate real gas equation of state for fluid dynamic analysis applications., *J. Fluids Eng.* 117 (1995) 277–281.
- [38] R. Span, Multiparameter Equations of State: An Accurate Source of Thermodynamic Property Data, Springer, Berlin, 2000.
- [39] R. Reid, J. Prausnitz, B. Poling, Properties of Gases and Liquids, 4th Edition, Mc.Graw–Hill Inc., 1987.
- [40] N. Spycher, K. Pruess, J. Ennis-King, A simulation program for non-isothermal multiphase reactive geochemical transport in variably saturated geologic media: applications to geothermal injectivity and CO<sub>2</sub> geological sequestration, *Geochim. Cosmochim. Acta* 67 (2003) 3015–3031.
- [41] D. Ambrose, Correlation and estimation of vapour-liquid critical properties. I. Critical temperatures of organic compounds, National Physical Laboratory, Teddington:NPL Rep. Chem. 92.
- [42] D. Ambrose, Correlation and estimation of vapour-liquid critical properties.II. Critical pressures and volumes of organic compounds, National Physical Laboratory, Teddington:NPL Rep. Chem. 98.
- [43] K. Joback, A unified approach to physical property estimation using multivariate statistical techniques, PhD dissertation, Department of Chemical Engineering, Massachusetts Institute of Technology, Cambridge, MA (1984).
- [44] K. Joback, R. Reid, Estimation of pure-component properties from group-contributions, *Chem. Eng. Comm.* 57 (1987) 233–243.
- [45] R. Fedors, A relationship between chemical structure and the critical temperature, *Chem. Eng. Comm.* 16 (1982) 149–151.
- [46] I. Owczarek, K. Blazej, Recommended critical temperatures. Part I. Aliphatic hydrocarbons, *J. Phys. Chem. Ref. Data* 32 (2003) 1411–1427. doi:[10.1063/1.1556431](https://doi.org/10.1063/1.1556431).
- [47] I. Owczarek, K. Blazej, Recommended critical temperatures. Part II. Aromatic and cyclic hydrocarbons, *J. Phys. Chem. Ref. Data* 33 (2004) 541–548. doi:[10.1063/1.1647147](https://doi.org/10.1063/1.1647147).
- [48] J. Prausnitz, R. Lichtenthaler, E. de Azevedo, Molecular thermodynamics of fluid-phase equilibria, Prentice Hall, 1986.
- [49] B. McBride, S. Gordon, M. Reno, Coefficients for calculating thermodynamic and transport properties of individual species, NASA Technical Memorandum 4513.
- [50] G. Froment, K. Bischoff, Chemical Reactor Analysis and Design, Wiley, New York, 1979.
- [51] C. Eckert, M. Boudart, On the use of fugacities in gas kinetics, *Chem. Eng. Sci.* 18 (1963) 144–147.
- [52] B. Buhre, L. Elliott, C. Sheng, R. Gupta, T. Wall, Oxy-fuel combustion technology for coal-fired power generation, *Prog. Energy Comb. Sci.* 31 (4) (2005) 283–307.
- [53] T. Wall, Y. Liu, C. Spero, L. Elliott, S. Khare, R. Rathnam, F. Zeenathal, B. Moghtaderi, B. Buhre, C. Sheng, R. Gupta, T. Yamada, K. Makino, J. Yu, An overview on oxyfuel coal combustion-State of the art research and technology development, *Chem. Eng. Res. Des.* 87 (8A) (2009) 1003–1016.
- [54] M. Saldana, G. B. Jr., Investigation of n-pentane pyrolysis at elevated temperatures and pressures in a variable pressure flow reactor, *J. Anal. Appl. Pyrol.* 118 (2016) 286–297.
- [55] F. Zhong, X. Fan, G. Yu, J. Li, Thermal cracking of aviation kerosene for scramjet applications, *Sci. China Series E: Tech. Sci.* 52 (9) (2009) 2644–2652.
- [56] B. Ruan, H. Meng, V. Yang, Simplification of pyrolytic reaction mechanism and turbulent heat transfer of n-decane at supercritical pressures, *Int. J. Heat Mass Tran.* 69 (2014) 455–463.
- [57] T. Kluyver, B. Ragan-Kelley, F. Pérez, B. Granger, M. Bussonnier, J. Frederic, K. Kelley, J. Hamrick, J. Grout, S. Corlay, P. Ivanov, D. Avila, S. Abdalla, C. Willing, Jupyter Notebooks—a publishing format for reproducible computational workflows, in: F. Loizides, B. Schmidt (Eds.), Positioning and Power in Academic Publishing: Player, Agents, and Agendas, IOS Press, Amsterdam, 2016, pp. 87–90.

- [58] <https://github.com/Cantera/cantera-jupyter/blob/master/reactors/NonIdealShockTube.ipynb>.
- [59] Python Software Foundation, <http://www.python.org>.
- [60] <https://github.com/Cantera/cantera/tree/master/interfaces/cython/cantera/examples/reactors/NonIdealShockTube.py>.

## Appendix A. Supplementary Material

### Appendix A.1. Tabulated Ignition Delay Measurements

Table A.1: Ignition delay time measurements for stoichiometric n-dodecane/air mixtures.

$p$ [atm]	$T$ [K]	$\tau$ [ $\mu$ s]	$p$ [atm]	$T$ [K]	$\tau$ [ $\mu$ s]	$p$ [atm]	$T$ [K]	$\tau$ [ $\mu$ s]
44.2	772	417	61.1	827	209	76.5	797	195
43.0	788	407	62.7	862	169	83.3	846	144
43.9	813	273	59.6	899	188	73.7	860	127
42.3	829	257	62.7	927	190	78.9	879	148
43.3	875	242	61.9	933	228	75.7	892	137
38.7	884	310	55.0	976	247	84.5	928	160
42.7	912	316	56.5	998	215	80.4	962	150
39.6	952	303	59.8	1030	149	77.2	1023	141
39.2	985	332	57.6	1069	120	81.8	1060	97
41.4	1023	260	64.6	1088	105			
38.3	1048	192	61.6	1121	70			
39.5	1063	179						
36.5	1130	108						
38.0	1161	65						

Table A.2: Ignition delay time measurements for  $\phi = 2.0$  n-dodecane/air mixtures.

$p$ [atm]	$T$ [K]	$\tau$ [ $\mu$ s]	$p$ [atm]	$T$ [K]	$\tau$ [ $\mu$ s]
39.0	800	256	62.6	818	202
38.8	801	253	61.5	851	147
38.3	811	230	60.6	888	154
41.4	836	209	59.7	926	155
43.2	846	191	61.1	967	178
42.2	925	234	58.2	983	172
37.8	932	250	57.4	1037	121
40.7	997	246	57.9	1086	78
36.3	1028	185	59.8	1101	75
36.9	1086	128			
38.6	1119	82			

### Appendix A.2. Publicly available, open source software tools

The shock tube reactor code used in this work will be made publicly available as part of the open-source CANTERA software package, both as a Jupyter-notebook [57] style tutorial [58], as a self-contained downloadable Python [59] module which can be edited and extended by the interested reader [60].

### Appendix A.3. Deriving the real gas equilibrium constant $K_{\text{eq}}$

Relating the forward and reverse rate constants in any reaction is achieved by assuming thermodynamic reversibility and requiring that the thermodynamic equilibrium state is identical to the kinetic equilibrium condition.

Thermodynamic equilibrium is evaluated according to  $\Delta G_i$ , the Gibbs free energy of reaction  $i$ :

$$\Delta G_i = \sum_k \nu_{k,i} \mu_k = \sum_k \nu_{k,i} \mu_k^\circ + RT \ln \left( \prod_k \alpha_k^{\nu_{k,i}} \right) = \Delta G_i^\circ + RT \ln \left( \prod_k \left( \frac{\gamma_k [X_k]}{[X_k^\circ]} \right)^{\nu_{k,i}} \right), \quad (\text{A.1})$$

Table A.3: Ignition delay time measurements for stoichiometric n-dodecane/air mixtures at O<sub>2</sub> concentrations of 15 and 13 mol-%.

0.811% n-dodecane/15% O <sub>2</sub> /N <sub>2</sub>			0.703% n-dodecane/13% O <sub>2</sub> /N <sub>2</sub>		
<i>p</i> [atm]	<i>T</i> [K]	$\tau$ [ $\mu$ s]	<i>p</i> [atm]	<i>T</i> [K]	$\tau$ [ $\mu$ s]
63.7	837	347	64.7	838	434
61.5	876	297	63.6	870	354
62.7	901	299	62.3	925	416
64.3	944	344	62.6	945	453
59.9	986	373	60.9	975	446
58.9	1009	275	59.9	1010	352
61.2	1059	188	61.2	1054	229
57.8	1075	141	59.3	1078	181
57.5	1109	114	57.8	1109	140
			58.5	1136	91

$$\Delta G_i = \Delta G_i^\circ + RT \ln \left( \prod_k \left( \frac{\gamma_k X_k}{p^\circ v} \right)^{\nu_{k,i}} \right) = \Delta G_i^\circ + RT \ln \left( \prod_k \left( \frac{\gamma_k RT}{p^\circ v} \right)^{\nu_{k,i}} \right) \quad (\text{A.2})$$

$$\Delta G_i = \Delta G_i^\ddagger + RT \ln \prod_k (X_k)^{\nu_{k,i}} + RT \ln \left( \prod_k \left( \frac{\gamma_k RT}{p^\circ v} \right)^{\nu_{k,i}} \right) \quad (\text{A.3})$$

$$\Delta G_i = \Delta G_i^\ddagger(T) + RT \ln \left( \prod_k \left( \frac{\gamma_k X_k}{p^\circ v} \right)^{\nu_{k,i}} \right), \quad (\text{A.4})$$

where  $\Delta G_i^\ddagger(T)$  is the temperature-dependent standard state Gibbs free energy of reaction *i*, calculated from NASA polynomial inputs, and where  $\nu_{k,i}$  is the net stoichiometric coefficient for species *k* in reaction *i*,  $\nu_{k,i} = \nu''_{k,i} - \nu'_{k,i}$ .

The chemical equilibrium condition is evaluated according to the net rate of progress for reaction *i*:

$$\dot{q}_i = \frac{1}{\gamma_i^*} \left( k_{f,i} \prod C_{ac,k}^{\nu'_{k,i}} - k_{r,i} \prod C_{ac,k}^{\nu''_{k,i}} \right). \quad (\text{A.5})$$

$$\dot{q}_i = \frac{1}{\gamma_i^*} \left( k_{f,i} \prod (\gamma_k [X_k])^{\nu'_{k,i}} - k_{r,i} \prod (\gamma_k [X_k])^{\nu''_{k,i}} \right) \quad (\text{A.6})$$

$$\dot{q}_i = \frac{1}{\gamma_i^*} \left( k_{f,i} \prod \left( \frac{\gamma_k X_k}{v} \right)^{\nu'_{k,i}} - k_{r,i} \prod \left( \frac{\gamma_k X_k}{v} \right)^{\nu''_{k,i}} \right) \quad (\text{A.7})$$

At equilibrium,  $\dot{q}_i$  must equal zero:

$$\dot{q}_i = 0 = \frac{1}{\gamma_i^*} \left( k_{f,i} \prod \left( \frac{\gamma_k X_k}{v} \right)^{\nu'_{k,i}} - k_{r,i} \prod \left( \frac{\gamma_k X_k}{v} \right)^{\nu''_{k,i}} \right) \quad (\text{A.8})$$

Therefore:

$$k_{f,i} \prod \left( \frac{\gamma_k X_k}{v} \right)^{\nu'_{k,i}} = k_{r,i} \prod \left( \frac{\gamma_k X_k}{v} \right)^{\nu''_{k,i}}, \quad (\text{A.9})$$

and

$$K_{eq,i} = \frac{k_{f,i}}{k_{r,i}} = \frac{\prod \left( \frac{\gamma_k X_k}{v} \right)^{\nu''_{k,i}}}{\prod \left( \frac{\gamma_k X_k}{v} \right)^{\nu'_{k,i}}} = \prod_k \left( \frac{\gamma_k X_k}{v} \right)^{\nu_{k,i}} \quad (\text{A.10})$$

Additionally, from thermodynamic equilibrium,  $\Delta G_i = 0$ :

$$\Delta G_i = \Delta G_i^\ddagger(T) + RT \ln \left( \prod_k \left( \frac{\gamma_k X_k}{p^\circ v} \right)^{\nu_{k,i}} \right) = 0. \quad (\text{A.11})$$

Therefore:

$$\prod_k \left( \frac{\gamma_k X_k}{\frac{p^\circ v}{RT}} \right)^{\nu_{k,i}} = \exp \left( -\frac{\Delta G_i^\ddagger(T)}{RT} \right), \quad (\text{A.12})$$

and

$$\prod_k \left( \frac{\gamma_k X_k}{v} \right)^{\nu_{k,i}} = \exp \left( -\frac{\Delta G_i^\ddagger(T)}{RT} \right) \prod_k \left( \frac{p^\circ}{RT} \right)^{\nu_{k,i}} = \exp \left( -\frac{\Delta G_i^\ddagger(T)}{RT} \right) \left( \frac{p^\circ}{RT} \right)^{\sum_k \nu_{k,i}} \quad (\text{A.13})$$

Combining Eqs. A.10 and A.13, we get:

$$K_{\text{eq},i} = \frac{k_{f,i}}{k_{r,i}} = \exp \left( -\frac{\Delta G_i^\ddagger(T)}{RT} \right) \left( \frac{p^\circ}{RT} \right)^{\sum_k \nu_{k,i}}. \quad (\text{A.14})$$

Regardless of any possible real gas effects on the individual rate constants  $k_{f,i}$  and  $k_{r,i}$ , we see that the ratio between the constants depends on temperature only. Note that this form is generally applicable to ideal and real gasses, but is equal to the commonly-used  $K_c$  coefficient only if an ideal gas is assumed.

#### Appendix A.4. Derivation of Redlich–Kwong Species Activity Coefficients

For the interested reader, we present a detailed derivation of the species activity coefficients presented in Eq. 31, above. The approach combines the Helmholtz energy departure function (Eq. 18), the definition of the chemical potential departure function (Eq. 29), and the definition of the activity coefficient (Eqs. 21 and 28). To make the derivative simpler, we first multiply Eq. 18 by  $n_T$  and convert molar volume  $v$  to total volume  $V = n_T v$  (because the differentiation in Eq. 29 is carried out at constant total volume):

$$n_T (a - a^\circ) = -RT n_T \ln \left( \frac{p^\circ (V - n_T b_{\text{mix}}^*)}{n_T RT} \right) - \frac{n_T a_{\text{mix}}^*}{b_{\text{mix}}^* \sqrt{T}} \ln \left( \frac{V + n_T b_{\text{mix}}^*}{V} \right), \quad (\text{A.15})$$

which can be re-written as:

$$n_T (a - a^\circ) = -RT n_T \ln \left( \frac{p^\circ V}{n_T RT} \right) - RT n_T \ln \left( \frac{V - n_T b_{\text{mix}}^*}{V} \right) - \frac{n_T a_{\text{mix}}^*}{b_{\text{mix}}^* \sqrt{T}} \ln \left( \frac{V + n_T b_{\text{mix}}^*}{V} \right). \quad (\text{A.16})$$

Let us then move the thermodynamic reference state total Helmholtz energy  $n_T a^\circ = \sum_i n_i (a_i^\ddagger + RT \ln X_i)$  to the right-hand side:

$$n_T a = \sum_i n_i (a_i^\ddagger + RT \ln X_i) - RT n_T \ln \left( \frac{p^\circ V}{n_T RT} \right) - RT n_T \ln \left( \frac{V - n_T b_{\text{mix}}^*}{V} \right) - \frac{n_T a_{\text{mix}}^*}{b_{\text{mix}}^* \sqrt{T}} \ln \left( \frac{V + n_T b_{\text{mix}}^*}{V} \right), \quad (\text{A.17})$$

where  $a_i^\ddagger$  is the standard-state, temperature-dependent molar Helmholtz energy for species  $i$ . This can be re-arranged as:

$$n_T a = \sum_i n_i a_i^\ddagger - RT \sum_i n_i RT \ln \left( \frac{p^\circ V}{n_i RT} \right) - n_T RT \ln \left( \frac{V - n_T b_{\text{mix}}^*}{V} \right) - \frac{n_T a_{\text{mix}}^*}{b_{\text{mix}}^* \sqrt{T}} \ln \left( \frac{V + n_T b_{\text{mix}}^*}{V} \right). \quad (\text{A.18})$$

Before taking the derivative, it is convenient to first establish that:

$$\frac{\partial a_{\text{mix}}^*}{\partial n_k} = \frac{2 \left( \sum_j a_{jk}^* X_j - a_{\text{mix}}^* \right)}{n_T}, \quad (\text{A.19})$$

and:

$$\frac{\partial b_{\text{mix}}^*}{\partial n_k} = \frac{b_k^* - b_{\text{mix}}^*}{n_T}, \quad (\text{A.20})$$

which follow directly from the fact that  $\frac{\partial n_T}{\partial n_k} = 1$  and therefore:

$$\frac{\partial X_j}{\partial n_k} = \begin{cases} n_T^{-1} - \frac{n_k}{n_T^2} = \frac{1-X_k}{n_T} & : j = k \\ -\frac{n_j}{n_T^2} = -\frac{X_j}{n_T} & : j \neq k. \end{cases} \quad (\text{A.21})$$

With this established, we can now take the derivative of Eq. A.18:

$$\begin{aligned} \mu_k &= \left( \frac{\partial (n_T a)}{\partial n_k} \right)_{T, V, n_{j \neq k}} \\ &= a_k^\dagger - RT \ln \left( \frac{p^\circ V}{n_k RT} \right) + RT - RT \ln \left( \frac{V - n_T b_{\text{mix}}^*}{V} \right) + n_T RT \frac{b_k^*}{V - n_T b_{\text{mix}}^*} \\ &\quad - \frac{a_{\text{mix}}^*}{b_{\text{mix}}^* \sqrt{T}} \ln \left( \frac{V + n_T b_{\text{mix}}^*}{V} \right) - \frac{2 \left( \sum_j a_{jk}^* X_j - a_{\text{mix}}^* \right)}{b_{\text{mix}}^* \sqrt{T}} \ln \left( \frac{V + n_T b_{\text{mix}}^*}{V} \right) \\ &\quad + \frac{a_{\text{mix}}^* (b_k^* - b_{\text{mix}}^*)}{b_{\text{mix}}^{*2} \sqrt{T}} \ln \left( \frac{V + n_T b_{\text{mix}}^*}{V} \right) - \frac{n_T a_{\text{mix}}^*}{b_{\text{mix}}^* \sqrt{T}} \frac{b_k^*}{V + n_T b_{\text{mix}}^*}. \end{aligned} \quad (\text{A.22})$$

Collecting terms, and converting  $V$  back to  $n_T v$ :

$$\begin{aligned} \mu_k &= a_k^\dagger + RT + RT \ln (X_k) - RT \ln \left( \frac{p^\circ (v - b_{\text{mix}}^*)}{RT} \right) + RT \frac{b_k^*}{v - b_{\text{mix}}^*} - \frac{a_{\text{mix}}^*}{b_{\text{mix}}^* \sqrt{T}} \left( \frac{b_k^*}{v + b_{\text{mix}}^*} \right) \\ &\quad + \frac{a_{\text{mix}}^* b_k^* - 2b_{\text{mix}}^* \sum_j a_{jk}^* X_j}{b_{\text{mix}}^{*2} \sqrt{T}} \ln \left( \frac{v + b_{\text{mix}}^*}{v} \right). \end{aligned} \quad (\text{A.23})$$

Recalling that  $\mu_k^\dagger = a_k^\dagger + RT$  and  $\mu_k^\circ = \mu_k^\dagger + RT \ln (X_k)$ :

$$\begin{aligned} \mu_k - \mu_k^\circ &= -RT \ln \left( \frac{p^\circ (v - b_{\text{mix}}^*)}{RT} \right) + RT \left( \frac{b_k^*}{v - b_{\text{mix}}^*} \right) - \frac{a_{\text{mix}}^*}{b_{\text{mix}}^* \sqrt{T}} \left( \frac{b_k^*}{v + b_{\text{mix}}^*} \right) \\ &\quad + \frac{a_{\text{mix}}^* b_k^* - 2b_{\text{mix}}^* \sum_j a_{jk}^* X_j}{b_{\text{mix}}^{*2} \sqrt{T}} \ln \left( \frac{v + b_{\text{mix}}^*}{v} \right). \end{aligned} \quad (\text{A.24})$$

Finally, we utilize the definition of the activity coefficient:

$$\begin{aligned} \mu_k - \mu_k^\circ &= RT \ln (\alpha_k) = RT \ln \left( \frac{\gamma_k [X_k]}{[X_k^\circ]} \right) \\ &= RT \ln (\gamma_k) + RT \ln \left( \frac{[X_k]}{[X_k^\circ]} \right) \\ &= RT \ln (\gamma_k) + RT \ln \left( \frac{X_k}{v} \right) - RT \ln \left( \frac{p^\circ X_k}{RT} \right) \\ &= RT \ln (\gamma_k) - RT \ln \left( \frac{p^\circ v}{RT} \right), \end{aligned} \quad (\text{A.25})$$

to calculate  $RT \ln (\gamma_k)$ :

$$\begin{aligned} RT \ln (\gamma_k) &= RT \ln \left( \frac{p^\circ v}{RT} \right) - RT \ln \left( \frac{p^\circ (v - b_{\text{mix}}^*)}{RT} \right) + RT \left( \frac{b_k^*}{v - b_{\text{mix}}^*} \right) - \frac{a_{\text{mix}}^*}{b_{\text{mix}}^* \sqrt{T}} \left( \frac{b_k^*}{v + b_{\text{mix}}^*} \right) \\ &\quad + \frac{a_{\text{mix}}^* b_k^* - 2b_{\text{mix}}^* \sum_j a_{jk}^* X_j}{b_{\text{mix}}^{*2} \sqrt{T}} \ln \left( \frac{v + b_{\text{mix}}^*}{v} \right). \end{aligned} \quad (\text{A.26})$$

This can be rearranged to provide:

$$RT \ln(\gamma_k) = RT \ln\left(\frac{v}{v - b_{\text{mix}}^*}\right) + RT \left(\frac{b_k^*}{v - b_{\text{mix}}^*}\right) + \frac{a_{\text{mix}}^* b_k^* - 2b_{\text{mix}}^* \sum_j a_{jk}^* X_j}{b_{\text{mix}}^{*2} \sqrt{T}} \ln\left(\frac{v + b_{\text{mix}}^*}{v}\right) - \frac{a_{\text{mix}}^*}{b_{\text{mix}}^* \sqrt{T}} \left(\frac{b_k^*}{v + b_{\text{mix}}^*}\right), \quad (\text{A.27})$$

which we can see is identical to Eq. 31.